Environ Model Assess (2013) 18:365–376
DOI 10.1007/s10666-012-9350-2

Application of Image Processing for Modelling Pyrite Oxidation in a Coal Washing Waste Pile

Mohammadhossein Sadeghiamirshahidi · Teimour Eslam Kish · Faramarz Doulati Ardejani

Received: 5 January 2012 / Accepted: 12 November 2012 / Published online: 22 November 2012

Abstract In this paper, an image processing method was applied to model the pyrite oxidation in the wastes of the Alborz Sharghi coal washing plant waste pile, northeast Iran. Pictures of polished sections created from the powdered samples of coal wastes were used to determine the amount of pyrite that remained at different depths of the waste pile. The amount of pyrite in the same samples also measured applying a method presented by ASTM, and the results were in very good agreement with the values calculated by the image processing method.

Keywords Image processing · Pyrite oxidation · Acid mine drainage generation · Coal washing waste pile

1 Introduction

Coal is one of the most widely used energy resources in developing and developed countries and can be regarded for many purposes as consisting of two classes of materials: organic components or macerals on one hand, and a range of minerals and other inorganic constituents, of which sulphide minerals are of the greatest environmental concern, on the other [1]. Because coal consists of two major solid components that are intimately associated, a complete, economically feasible separation of this undesirable inorganic fraction from the desirable organic fraction can never be achieved, and even a well-cleaned coal will contain a significant fraction of inorganics. Consequently, the presence of inorganics in coal utilisation cannot be avoided and the resolution or minimisation of many coal-utilisation environmental problems requires that the behaviour of the inorganic components during utilisation be well understood [2]. Information about the abundance, distribution and origin of sulphur in coal is important while sulphur oxides released in coal combustion are a major source of acid rain [3]. On the other hand, before using the coal, some operations dependent upon the purpose of consumption, such as coal washing, are applied to meet the best possible quality. These operations cause producing tons of sulphide-rich waste materials piled in the vicinity. Oxidation of sulphide minerals (in particular pyrite as the most abundant sulphide mineral) resulting from the exposure of these minerals to both oxygen and water [4] is the most important factor in the generation of acid mine drainage (AMD) which has detrimental environmental impact on aquatic systems. Hence, it is an important task to determine sulphide minerals especially pyrite in such waste dumps.

Many investigations have been carried out to consider the amount of pyrite in coal and/or in its waste piles. A method presented by ASTM [5] is the most reliable and widely used method to determine organic sulphur from the non-organic sulphur in coal and/or its wastes. In this method, hydrochloric acid (HCl) is used to dissolve sulphates and then the pyrite is extracted from the remained acidic aqueous solution using nitric acid (HNO_3). The ASTM method is a cumbersome approach and many researchers are seeking to find an easier, cost-effective and accurate way to quantitatively analyse the pyrite in coal and its wastes [5].

Aylmer and Rowe in 1984 developed a new simultaneous method for the determination of pyrite content and proximate analysis in coal [6]. It combines thermogravimetry and thermomagnetometry and utilises inert, oxidising and

M. Sadeghiamirshahidi (✉) · T. Eslam Kish
Department of Mining and Metallurgy Engineering, Amirkabir University of Technology (Tehran Polytechnic), Tehran, Iran
e-mail: m.h.sadeghi@aut.ac.ir

T. Eslam Kish
e-mail: t.eslamkish@aut.ac.ir

F. Doulati Ardejani
School of Mining, College of Engineering, University of Tehran, Tehran, Iran
e-mail: fdoulati@ut.ac.ir

reducing gases. There are two situations in which this method has more accurate results compared to the ASTM approach: first when pyrite is totally surrounded by acid-insoluble organic material, and second, where significant amounts of pyrite have weathered to $FeSO_4$ [6].

High-resolution time-of-flight secondary ion mass spectrometry (TOF-SIMS) was used by Shifeng et al. [7] to investigate the chemical composition of various pyrite forms in a coal seam. Five types of pyrite occurrences, including bacteriogenic, framboidal, massive, cell-filling and fracture-filling pyrites, were observed and identified in the coal seam under reflected-light microscope, a scanning electron microscope or monitor of the TOF-SIMS instrument [7].

Trudy [8] used sulphur X-ray near-edge absorption spectroscopy to direct determination of pyrite content in Argonne premium coals. They used this characterisation technique in conjunction with others like X-ray photoelectron spectroscopy to provide valuable information about chemical and thermal transformation. They showed that particle-size effects are responsible for attenuating the pyrite signal for high-pyrite-containing Argonne premium coals.

An overview of analytical methods for determination of inorganic constituents in coal is presented by Huggins [2]. In this research, Huggins reviewed analytical methods for measuring inorganics in coal on three fronts: (1) methods for determining elemental concentrations, (2) methods for determining the mineralogy of coals (including pyrite) and (3) methods for determining modes of occurrence of trace elements in coal. Huggins [2] explained that there has been much use of XRD for examination of the mineral matter in coals. The XRD technique can be performed both qualitatively and, with significant care, reasonably quantitatively. Usually, to ensure best results, it is recommended to work on low-temperature ash (LTA). Generally, determination of major minerals in LTA of coal are made based on a calibration procedure that involves use of an internal standard, such as calcium fluoride, CaF_2, and comparison of the height or area ratios of diffraction peaks from minerals in the coal relative to those of CaF_2 against a calibration curve based on the same peak–height or peak–area ratios for mixtures of CaF_2 and specific minerals (e.g. quartz, pyrite, kaolinite, etc.) of known composition [2]. Under optimum circumstances, errors of estimation based on conventional XRD of between ±5% and 10 % can be achieved, although individual minerals may be estimated more precisely using a specialised method [2]. Such methods have included the estimation of pyrite in Spanish coals [9]. Huggins further explained that scanning electron microscopy (SEM) has often been used qualitatively and occasionally semi-quantitatively to examine mineral matter in coal [2].

The great potential of SEM for recognising mineral occurrences and semi-quantitatively determining their relative abundances in coal, even for many trace elements, can be clearly seen in the detailed studies carried out by Finkelman [10, 11]. The various SEM-based methods that have been developed for quantifying coal mineralogy can be grouped under the heading of computer-controlled scanning electron microscopy (CCSEM). Such techniques have also been referred to as SEM automated image analysis (SEM-AIA) [2].

A novel instrument, similar in concept to the CCSEM method, but combining automated image analysis with an electron microprobe rather than an SEM, has been described by Shirazi et al. [12].

As a result of the much higher generation of X-rays produced from samples under the electron beam in a microprobe compared to that in an SEM, the atomic number contrast of different minerals is significantly better in the microprobe. For example, it is possible to discriminate between marcasite and pyrite, despite the fact that they have identical average atomic numbers, because of the difference in specific gravity of the two minerals that results in discernibly different contrast levels in the back-scattered electron image [2]. At the end, comparison of determinations of weight percent pyrite in Argonne premium coal samples as determined by X-ray diffraction, CCSEM and Mossbauer spectroscopy is shown by Huggins [2]. There appear to be only XRD and CCSEM methods that are currently in use for determining mineral matter (including sulphide minerals especially pyrite) in coal. CCSEM methods are best performed on polished sections of pulverised and homogenised coal, and will supply information on significantly more minerals than XRD methods [2].

In all these methods, especially in the ASTM approach as the most widely used method, a huge preparation process is needed and it takes lots of time. Furthermore, in most of these methods, the pyrite content is measured indirectly.

In addition to these investigations trying to determine the amount of pyrite content, several mathematical models have been developed to predict the pyrite oxidation and AMD generation (e.g. [14–21]).

A one-dimensional model for pyrite oxidation and leaching processes of the oxidation products was developed by Cathles and Apps [14]. Temperature dependence, oxygen balance and air convection effects were the parameters used for this model of which air convection was assumed to be the main mechanism of oxygen transport through the dump to oxidise ferrous ion in the presence of iron-oxidising bacteria.

Jaynes et al. [15] developed a one-dimensional finite difference model called POLS for simulating the long-term oxidation of pyrite and AMD generation from reclaimed coal strip mines. The model takes into consideration pyrite oxidation by both direct oxygen and ferric iron within the waste. It was assumed that pyrite oxidation is controlled by first-order kinetics and the rate of diffusion of oxidant into the reacting particles. The model further assumes that the

oxidation products are removed from the reclaimed strip mine by percolating surface water. The role of groundwater in transporting the oxidation products was neglected [21].

Davis and Ritchie [17] presented a one-dimensional mathematical model for pyrite oxidation within the White's overburden dump at Rum Jungle, Australia, where diffusion of oxygen to the reaction sites is the rate-limiting factor. The modelling was carried out in a two-stage approach with, first, the diffusion of oxygen into the pore space of the dump and, second, a shrinking core model to describe the diffusion of oxygen into the individual particles through the oxidised coating that forms around the unreacted core of the particles.

The numerical model developed by Elberling et al. [18] can be used to simulate pyrite oxidation in tailings. The model was formulated by combining the effect of oxygen diffusion to a depth where oxidation takes place with first-order kinetics with respect to oxygen. The rate of pyrite oxidation in the model is based on the continuity relationship for oxygen with both oxygen transport through the tailings and the consumption of oxygen at the surface of the sulphide minerals grains.

Gerke et al. [24] modelled the impact of physical and chemical heterogeneity on solute leaching in pyritic overburden mine wastes. The major processes considered consist of variably saturated water flow, oxygen diffusion, shrinking core kinetics of pyrite oxidation, multi-component reactive solute transport and geochemical equilibrium reactions between aqueous and mineral components.

Lengke et al. [13] applied net carbonate value (NCV), paste pH, net acid generation (NAG) pH and humidity cell test (HCT) to improve screening run-of-mine waste. The NCV classification is incapable of accurately predicting the potential of acid generation in those cases where acid is generated by soluble aluminium and iron sulphates. Hence, the HCTs were assessed for net alkalinity, pH, a molar ratio of (Ca+Mg/sulphate) and carbonate dissolution versus pyrite oxidation rates for HCTs over a 20-week period and/or the HCT forecast after 20 weeks. Results of HCTs in comparison with combination of NCV, paste pH and net acid generation (NAG) pH were used to predict the potentiality of acid generation in mine wastes.

Doulati Ardejani et al. [20] presented a combined mathematical–geophysical model for prediction of pyrite oxidation. Effective diffusion coefficient, pyrite fraction, bulk density of waste, molar density of pyrite within particle, surface area of pyrite per unit volume of waste, diameter of particles, first-order rate constant for oxygen, diffusion coefficient of oxygen in water, recharge value and waste column depth were considered in their simulation.

The multiplicity of the factors that affect the pyrite oxidation complicates the model development using classical techniques. In other words, in these classical techniques, it is necessary to obtain a variety of different factors to develop the model. Multiple experiments which are needed to measure these factors take long time. In addition, so many experiments increase the probability of having more errors in the calculations. Furthermore, in these classical methods some data distributions and boundary conditions must be assumed which are not necessarily true in nature.

In this research, we introduce an image processing approach as a new direct method for determination of the pyrite content with a very simple preparation process. It is also a very powerful and reliable tool to predict the pyrite oxidation process within the wastes produced by the Alborz Sharghi active coal washing plant, northeast Iran. Unlike other modelling techniques, our method makes no prior assumptions concerning the data distribution. For this purpose, MATLAB software was used. In the presence of oxygen, pyrite is oxidised to form Fe^{2+}, SO_4^{2-} and H^+, and the amount of the pyrite within the waste decreases subsequently. According to this fact, we measured the amount of pyrite that remained in the wastes at different depths to investigate the rate of pyrite oxidation.

2 Site Description

The Alborz Sharghi coal field consists of sandstone, thin bedded coaly shale of the Shemshak formation and alluvial deposits. The extracted coal from the region is washed in the Alborz Sharghi coal washing plant which is located northeast of Damghan and 57 km from Shahrood [21]. The washing process is carried out either using a jig machine or in a flotation cell. The wastes of each method are dumped separately. In the present study, samples were cut out of the jig machine waste pile. The location of our study area and a schematic view of the pile as well as the sampling locations are shown in Fig. 1. As it is well illustrated, samples were collected from three different locations.

3 Materials and Methods

3.1 Pyrite Oxidation and AMD Generation

Details of pyrite oxidation and the formation of AMD are described in Atkins and Pooley [22]. The chemical reaction describing pyrite oxidation by O_2 is expressed by Eq. 1:

$$FeS_2 + 7/2\ H_2O \rightarrow Fe^{2+} + 2\ SO_4^{2-} + 2\ H^+ \quad (1)$$

Fe^{2+} which is produced by the pyrite oxidation (Eq. 1) forms Fe^{3+} during the following reaction:

$$Fe^{2+} + 1/4\ O_2 + H^+ \rightarrow Fe^{3+} + 1/2\ H_2O \quad (2)$$

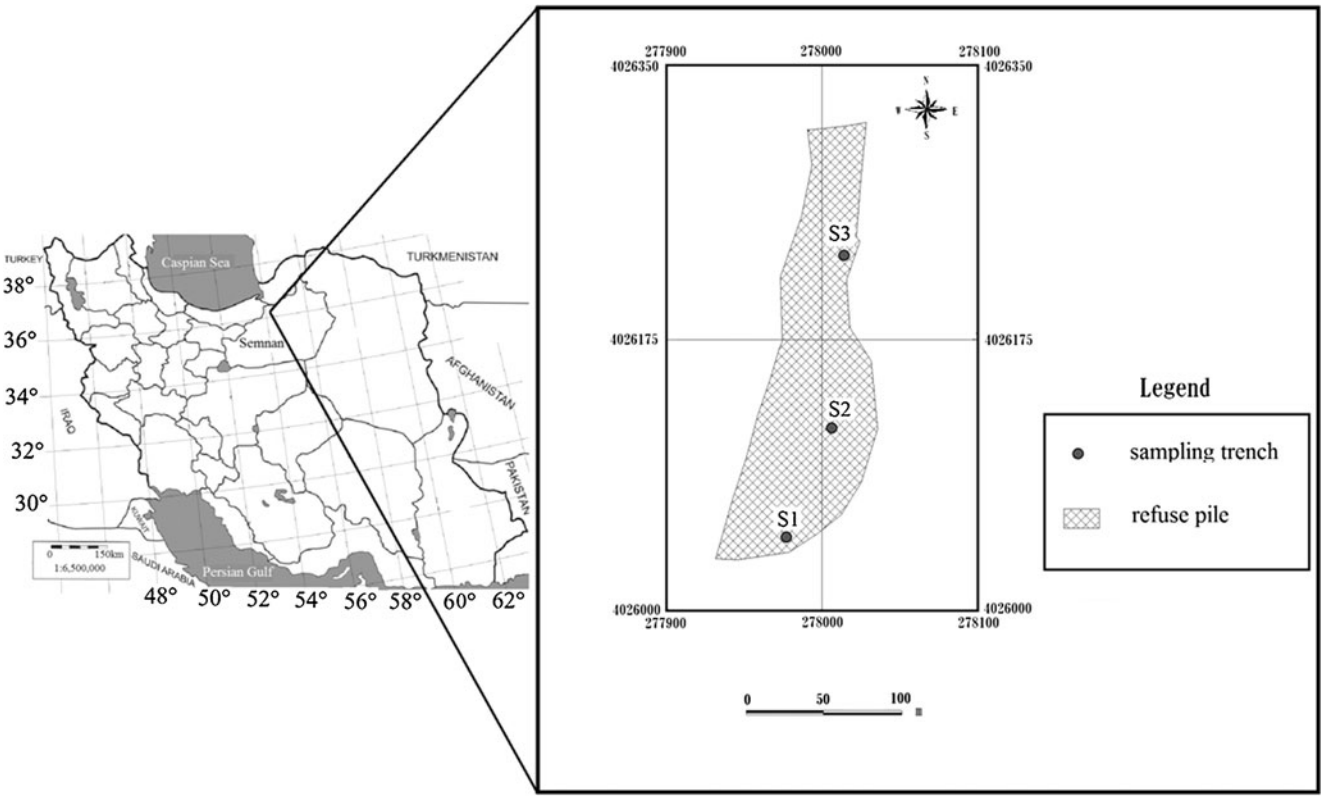

Fig. 1 The location of study area and a schematic view of refuse pile including the position of trenches (modified from Sadeghiamirshahidi et al. [28])

Fe^{3+} produced by the oxidation of ferrous iron (Eq. 2) may react with pyrite to produce additional Fe^{2+}, SO_4^{2-} and H^+ according to Eq. 3 [22]:

$$FeS_2 + 14\ Fe^{3+} + 8\ H_2O \rightarrow 15\ Fe^{2+} + 2\ SO_4^{2-} + 16H^+ \quad (3)$$

In the presence of the lithotrophic bacteria *Acidithiobacillus ferrooxidans*, this reaction (Eq. 3) has an important role in pyrite oxidation. Figure 2 shows a schematic diagram describing pyrite oxidation and subsequent pollutants leaching from a waste dump. This figure conceptually identifies oxygen diffusion, pyrite oxidation in waste materials and the transportation of oxidation products through coal waste materials [23].

3.2 Sampling and Measuring the Pyrite Content

Five samples were collected from trench 1 and six samples were collected from each one of two other trenches totalling 17 samples. Samples were extracted from different depths of the trenches. For all trenches, the total depth of sampling was 2.0 m and the sampling interval was 0.4 m. The first sample of trench 1 was cut out of the depth of 0.4 m and for two other trenches the first sample was taken from the waste pile surface. Samples were oven dried at 105 °C for 72 h in the mineral processing laboratory at Amirkabir University of Technology, Tehran, Iran. Then grinding was conducted applying a jaw crusher, cone crusher and roll crusher, respectively. For measuring the pyrite content that remained in the wastes of different depths, the method presented by ASTM was employed [5]. For this purpose, we needed to achieve the maximum grain size of 0.074 mm; therefore, sieve analysis was done using five sieves with different sizes (0.595, 0.250, 0.149, 0.105 and 0.074 mm). After obtaining the required grain size of below 0.074 mm, hydrochloric acid (HCl) was used to dissolve sulphates and the pyrite was then extracted from the remained acid aqueous solution using nitric acid (HNO_3). An AA-670 Shimadzu atomic absorption at Shahrood University of Technology was used to measure iron in the solution. It was eventually employed to determine the pyrite content that remained in the waste particles. The content of pyrite that remained within the waste particles from different depths of the refuse pile is shown in Table 1. The results show that the pyrite content increases with depth, which is related to the decrease of oxygen diffusion with depth.

3.3 Image Processing Approach

For measuring the pyrite content, polished sections were created applying a cold mounting method from powder under 0.105 mm. Some of the pictures of polished sections

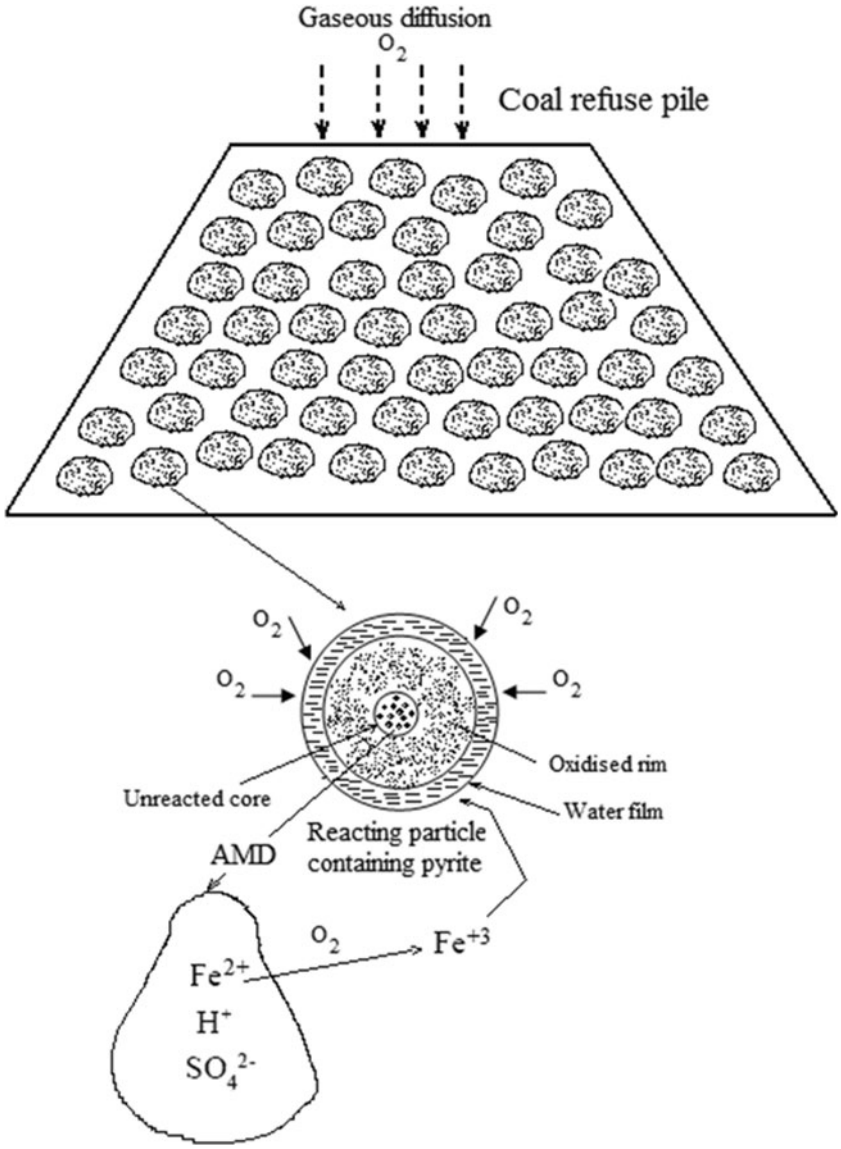

Fig. 2 Schematic diagram representing pyrite oxidation and pollutants leaching from a coal refuse pile (modified from Doulati Ardejani et al. [20])

Table 1 Pyrite content remained in the wastes at different depths of the pile

Depth (m)	Pyrite content remained (%)								
	Sampling location								
	S1			S2			S3		
	ASTM	IP[a]	Relative[b] error (%)	ASTM	IP[a]	Relative[b] error (%)	ASTM	IP[a]	Relative[b] error (%)
0	–	–	–	0.379	0.43	13.45	0.292	0.32	9.58
0.4	0.360	0.40	11.11	0.48	0.54	12.50	0.396	0.43	8.58
0.8	0.490	0.55	12.24	0.578	0.59	2.07	0.481	0.51	6.02
1.2	0.596	0.62	4.02	0.64	0.60	6.25	0.557	0.52	6.64
1.6	0.643	0.63	2.02	0.689	0.63	8.56	0.612	0.56	8.49
2.0	0.689	0.66	4.20	0.735	0.68	7.48	0.65	0.60	7.69

[a] Image processing method

[b] Relative error (%) $= (|\mathrm{ASTM} - \mathrm{IP}|/\mathrm{ASTM}) * 100$

captured under a microscope (OLYMPUS HQ-2553) are shown in Fig. 3. There are two objects of interest in all images: the first object is pyrite which is observed in yellow colour through all images and the second one is objects in black colour representing other materials in coal wastes despite pyrite. The grey colour, observed in images, is related to the resins, polyester and hardener used in creating the polished sections. MATLAB software was applied to segment these two objects and measure the amount of pyrite in these images. There are four well-known kinds of pictures in MATLAB consisting of binary images (also known as bi-level images), indexed images (also known as pseudo-colour images), greyscale images (also known as intensity, grey scale, or grey level images) and true-colour images (also known as RGB image). The pictures of polished sections lie in the fourth groups (true-colour or RGB images).

3.3.1 Digital True-Colour Images

A digital image can be defined as a function, $f(x, y)$, where x and y are spatial coordinates, and the amplitude of f at any pair of coordinates (x, y) is called intensity of the image at that point. When all x, y and the amplitude values of f are finite and discrete quantities, the image is called a digital image. Note that a digital image is composed of a finite number of elements (pixels) and each pixel has a particular location (x, y) and value (f) [25]. Digital colour images can be assumed as three digital images, each image showing the intensity of one of the three main colours (red, green and blue). Therefore, each pixel of a digital colour image is specified by five values (x, y, R, G, B) where x and y denote the location of pixel in the image and R, G and B are the intensity of red, green and blue colour, respectively, in that

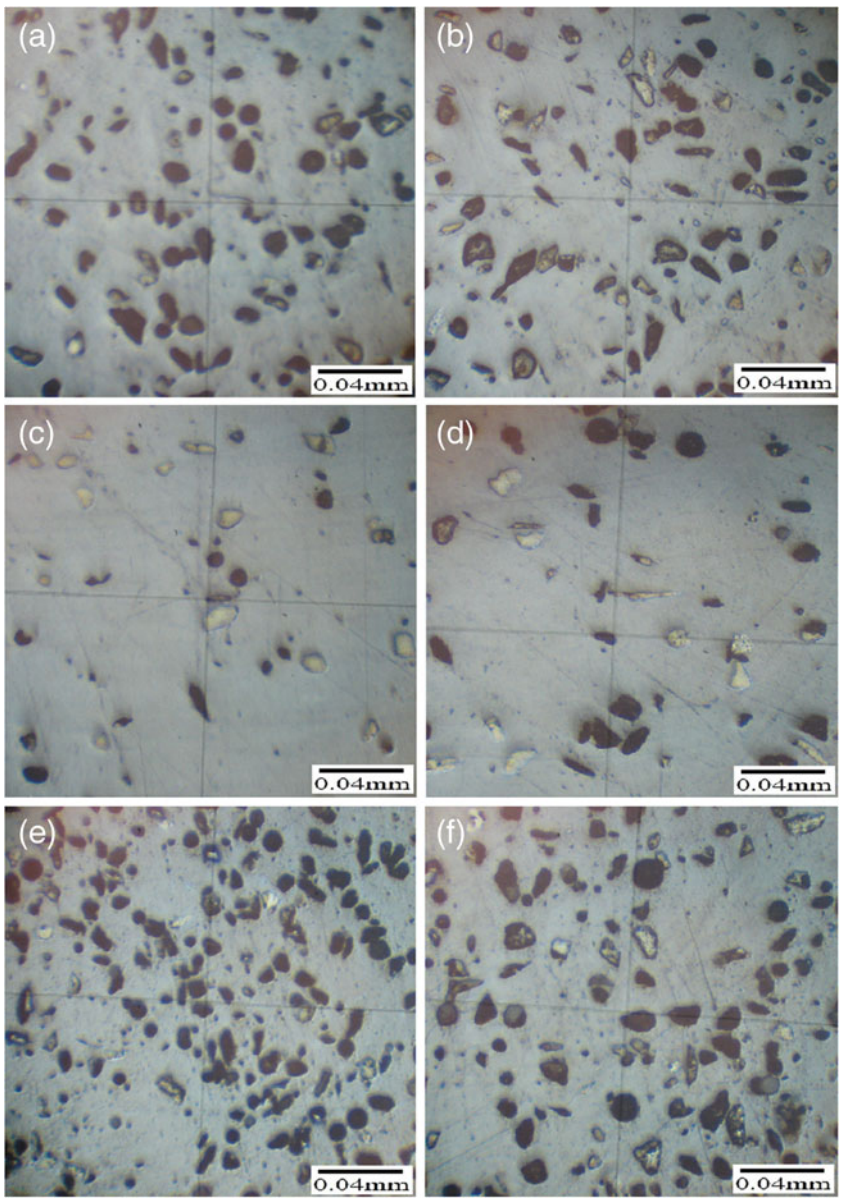

Fig. 3 Selection of pictures of polished sections. **a** Sample from trench 1, 0.8 m depth; **b** sample from trench 1, 1.2 m depth; **c** sample from trench 2, 0.8 m depth; **d** sample from trench 2, 1.2 m depth; **e** sample from trench 3, 0.8 m depth; **f** sample from trench 3, 1.2 m depth

location. Colour images in MATLAB are handled as an M× N×3 array of colour pixels with different data classes. The data class identifies the range of R, G and B values. Our pictures are of class uint8 (unsigned 8-bit integer) and the range of values is [0, 255].

3.3.2 Image Enhancement

As can be seen in Fig. 3, pictures are prone to some noises. There are large numbers of black spots and lines that are not really waste materials but have the same RGB values. They are considered as noises and must be excluded before any analysis is conducted. For this purpose, some morphological operations were applied. In a morphological operation, the input image is converted to an output image of the same size using a structuring element. The structuring element introduces a neighbourhood for each pixel in the input image in which the values of pixels in input and output images are compared. The values of pixels in the output image are obtained from this comparison. The best results can be achieved by changing the size and shape of the neighbourhood. Dilation and erosion are considered to be the most basic morphological operations [26]. In this study, dilation was applied in the operations. In the morphological dilation operation, the state of any given pixel in the output image is determined by applying a rule to the corresponding pixel and its neighbours in the input image. The rule is that the value of the output pixel is the maximum value of all the pixels in the neighbourhood of input pixel. A necessary part of the dilation process is to apply structuring element to explore the input image. A structuring element is a kind of matrix with any arbitrary shape and size that incorporates only 0's and 1's values. The neighbourhood is defined by the pixels having values of 1 [26].

Dilation of an RGB image by structuring element C, denoted (RGB⊕C), is defined as:

$$(\mathrm{RGB}\oplus\mathrm{C})(s,t)=\begin{cases}(\mathrm{R}\oplus\mathrm{C})(s,\ t)=\max\{\mathrm{R}(\mathrm{s}-\mathrm{x},\ \mathrm{t}-\mathrm{y})+\mathrm{C}(\mathrm{x},\ \mathrm{y})|(\mathrm{s}-\mathrm{x}),\ (\mathrm{t}-\mathrm{y})\in \mathrm{D_R};\ (\mathrm{x},\ \mathrm{y})\in \mathrm{D_C}\}\\ (\mathrm{G}\oplus\mathrm{C})(s,\ t)=\max\{\mathrm{G}(\mathrm{s}-\mathrm{x},\ \mathrm{t}-\mathrm{y})+\mathrm{C}(\mathrm{x},\mathrm{y})|(\mathrm{s}-\mathrm{x}),\ (\mathrm{t}-\mathrm{y})\in \mathrm{D_G};\ (\mathrm{x},\ \mathrm{y})\in \mathrm{D_C}\}\\ (\mathrm{B}\oplus\mathrm{C})(s,\ t)=\max\{\mathrm{B}(\mathrm{s}-\mathrm{x},\ \mathrm{t}-\mathrm{y})+\mathrm{C}(\mathrm{x},\ \mathrm{y})|(\mathrm{s}-\mathrm{x}),\ (\mathrm{t}-\mathrm{y})\in \mathrm{D_B};\ (\mathrm{x},\ \mathrm{y})\in \mathrm{D_C}\}\end{cases} \quad (4)$$

where R(s, t) denotes the intensity value of red colour, at the pixel (s, t) with the spatial coordinates s and t, of the RGB image, G(s, t) represents the intensity value of green colour at the pixel (s, t), and B(s, t) is the intensity value of the blue colour at pixel (s, t). D_R, D_G, D_B and D_C represent the domain of red colour intensity values, green colour intensity values, blue colour intensity values and structuring element matrix values, respectively. It was found that a flat, disk-shaped structuring element, with a radius of 2, has the best results for enhancing our images (Fig. 4). In morphological operation, the origin of the structuring element, its centre element, is positioned over the pixel of interest in the input image. For pixels at the edge of an image, parts of the neighbourhood defined by the structuring element can extend past the border of the image. To process border pixels, a value is assigned to these undefined pixels, as if the image had padded with additional rows and columns. The value of these padding pixels for dilation operation was determined by applying this rule that pixels beyond the image border are assigned the minimum value afforded by the data type [26]. Figure 5a and b illustrates the picture of the polished section of one of the samples (sample c) before and after the dilation operation as an example to show how this morphological operation can improve the quality of images.

After dilating the images, the saturation and the hue of the yellow colour of pyrite in different parts of each picture widely vary. In addition, the RGB values of pyrite in the pictures overlap the RGB values of background in some parts which make it impossible to separate them. Enhancing colour separation using de-correlation stretching was applied to overcome

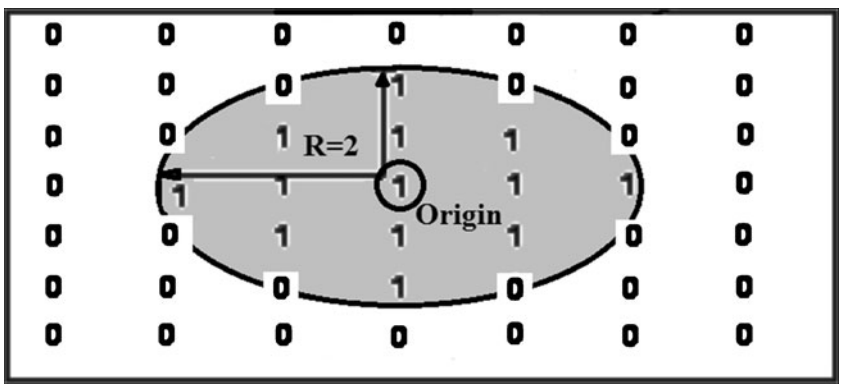

Fig. 4 Schematic view of disk-shaped structuring element with a radius equal to 2 for dilation operation (modified from Image Processing Toolbox™ user's guide, 2008 [26])

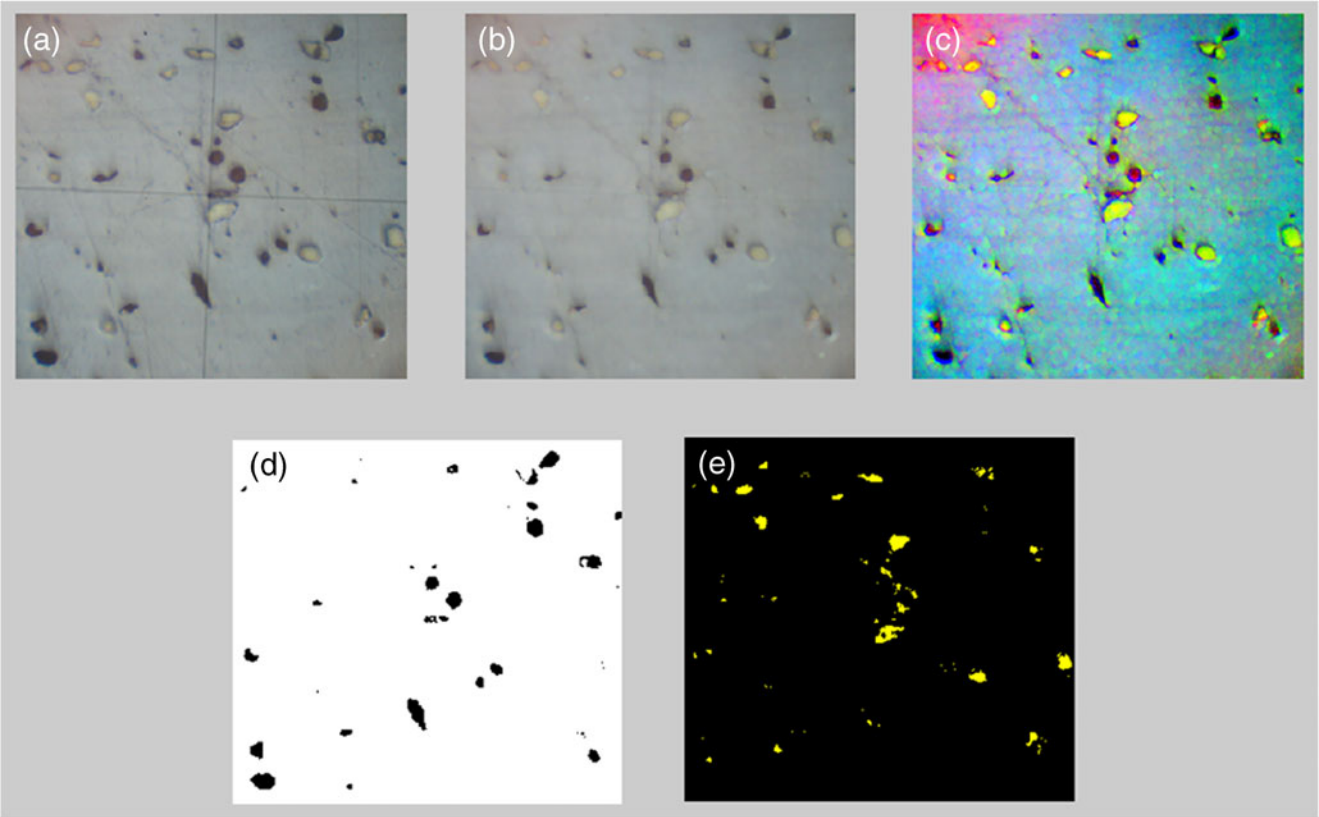

Fig. 5 Pictures of a polished section before and after image processing operations. **a** Original image, **b** dilated image, **c** colour separation enhanced image, **d** image which shows the counted pixels as black and uncounted pixels as white to check that the black objects in original image segmented correctly, **e** image which shows the counted pixels as yellow and uncounted pixels as black to check that the yellow objects in original image segmented correctly (sample from a depth of 0.8 m of trench no. 2; c in Fig. 3)

this problem. De-correlation stretching enhances the colour separation of an image with significant band-band correlation. The exaggerated colours improve visual interpretation and make feature discrimination easier. The number of colour bands, NBANDS, in the image is usually three. But de-correlation stretching can be applied regardless of the number of colour bands. The original colour values of the image are mapped to a new set of colour values with a wider range. The colour intensities of each pixel are transformed into the colour eigenspace of the NBANDS-by-NBANDS covariance or correlation matrix, stretched to equalise the band variances, then transformed back to the original colour bands [26].

The de-correlation stretch program enhances the colour separation in images with high interchannel correlation. In this program, three channels of each pixel are assumed as three vectors. These vectors are transformed to a new space using a linear transformation process which removes the correlation among the vectors in the transformed space. This is similar to rotating the coordinate system of the original vector space. In this rotated space, variances of the vectors are normalised in order to stretch the contrast. The vectors are then rotated back to the original coordinate system. The de-correlation stretched output can be produced from the input image by a single mathematical operation. Although the relative sense of hue, saturation and intensity of the input image are preserved, pixels are well distributed among all possible colours in the output image [27]. The algorithm is briefly described below to better understanding the method.

Initially, a grid of pixels is chosen by sub-sampling the image at regular intervals. This grid is supposed to form a representative sample of all 'good' surface pixels found within the scene. Pixels which are marked as 'bad data' are omitted from the grid. Sub-sampling may result in insufficient usable pixels. In that case, all 'good' pixels are incorporated in the grid. The sampled pixels are used to calculate the covariance matrix for the three channels [27]:

At first, nine sums which are required to determine the covariance are computed as below:

For l=1, 3; m=1, l, and sampling n pixels,

$$SUM\,X_{l,m} = \sum P_{k,l} * P_{k,m} \tag{5}$$

$$SUM_l = \sum p_{k,l} \tag{6}$$

where $P_{k,l}$ denotes the value of the kth pixel for channel l.

The following equation is used to calculate the elements of the covariance matrix:

$$Cov_{l,m} = (1/(n-1)) * \left[SUM\, X_{l,m} - (1/\mathrm{n}) * \mathrm{SUM_l} * \mathrm{SUM_m}\right] \quad (7)$$

The following expression can be written for correlation matrix elements:

$$Corr_{l,m} = Cov_{l,m} / \left[\left(Cov_{l,l} Cov_{m,m}\right)^{(1/2)}\right] \quad (8)$$

The correlation matrix (or, optionally, of the covariance matrix) is used to calculate the eigenvectors and eigenvalues of the system. The reciprocal of the square root of each element in the eigenvalues vector multiplied by the desired standard deviation for the output image channels is called the normalisation vector. Although the desired standard deviation for true normalisation is one, the standard deviation is set to 50 in order to yield output values in the appropriate range for eight-bit pixels. The final transformation matrix, **T**, is composed from the eigenvectors matrix and the normalisation vector. This is performed using the following matrix multiplication [27]:

$$\mathbf{T} = \mathbf{R^t s\, R} \quad (9)$$

where **R** is referred to the matrix of eigenvectors (also known as rotation matrix) and **s** denotes the normalisation vector (or stretching vector).

The output image values must lay in the 0 to 255 dynamic ranges of eight-bit data. An offset vector is needed to reposition these values in the desired range. Hence, the transformation is applied to a vector of the means of the input channels and the result is used to calculate the offsets. Therefore, each output pixel is derived from applying the final transformation matrix and offset vector, respectively [27]. Figure 5a and c compares the image before and after colour separation enhancement. As it is obvious in this figure, now it is possible to segment pyrite with sharp yellow colour from the background. Figure 6 demonstrates the colour scatterplot of original image, dilated image and de-correlation stretched image. According to this figure, it can be realised that the colour values in the original image and dilated image have a very tight range, but the colour separation enhanced image has the wider range of colour values.

3.3.3 Measuring the Amount of Pyrite (Yellow Objects) and Other Materials (Black Objects) in the Images

To measure the amount of the black objects in images (all materials in wastes despite pyrite), the original images were used for the reason that the range of RGB values of these black objects does not overlap the range of other objects.

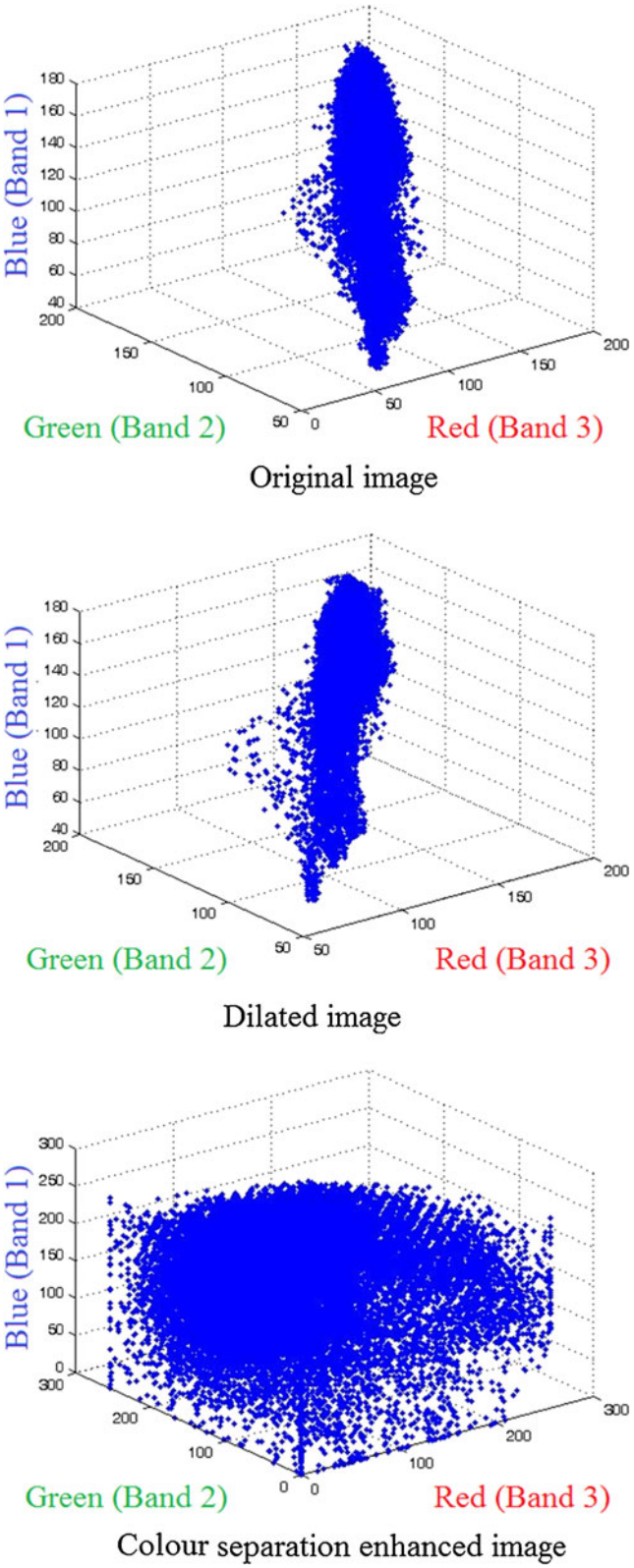

Fig. 6 Colour scatterplot of original image, dilated image and de-correlation stretched image

The number of pixels with the RGB values between the range of interest (0<R<125; 0<G<100; 0<B <110) were

counted. To check that the objects were accurately segmented, we assigned the RGB values of pixels which are counted to 0 (black colour) and values of uncounted pixels to 255 (white colour). Then the picture with the new RGB values was compared to the original image (Fig. 5d). There was a good agreement between black objects in original image and black objects in our new image (counted pixels—black, uncounted pixels—white). To measure the amount of yellow objects (pyrite), the colour separation enhanced image was used. Pixels with the RGB values between our range of interest ($130<R<255$; $130<G<255$; $0<B<60$) were counted. To check that we segmented the yellow objects correctly, we assigned the RGB values of pixels which are counted to 255, 255 and 0, respectively (yellow colour), and values of uncounted pixels to 0 (black colour). The picture with new RGB values was then compared to the original images (Fig. 5e). As it is shown in this figure, there is a good agreement between segmented yellow objects in the new image and the original image (counted pixels—yellow, uncounted pixels—black).

4 Results and Discussion

All polished sections were analysed after removing noises and enhancing colour separation. Therefore, the amount of yellow and black objects (pyrite and other materials despite pyrite, respectively) in all pictures was computed. The amount of pyrite in each sample was computed using the following equation:

$$Py_{(\%)} = \frac{k \times y}{y + b} \times 100 \tag{10}$$

where $Py_{(\%)}$ is the percentage of pyrite in each sample, y represents the amount of yellow objects (number of yellow pixels in picture 6c), b denotes the amount of black objects (number of black pixels in picture 6b) and k is a constant coefficient.

To measure the pyrite content using the ASTM approach, as a standard method, the powder size of 0.074 mm is often used. Since the powder size of 105 μm was used in creating polished sections, hence it should be considered in the computations. The hardness of the waste materials affects our computations in two ways: first, according to the higher hardness of pyrite, coal wastes are ground easier and the amount of them in finer materials (powder finer than 0.074 mm) is higher compared to the coarser materials (powder finer than 0.105 mm) while the condition is reversed for the pyrite. Second, during the polishing process of sections, some coal waste particles could be removed according to their low hardness. It should be added that in the ASTM approach, the weight percent of pyrite is measured and according to the difference between the density of pyrite and other waste materials there is a distinction between the weight percent (measured in ASTM approach)

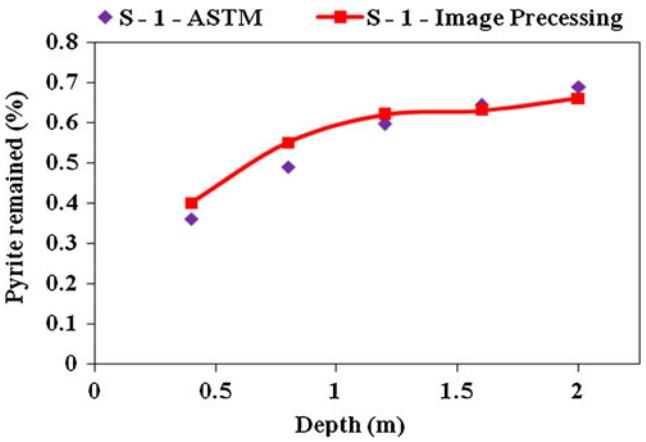

Fig. 7 Comparison of the image processing results (*solid line*) with the measured values (*dots*) for the amount of pyrite remained within the waste particles versus depth in trench no. 1

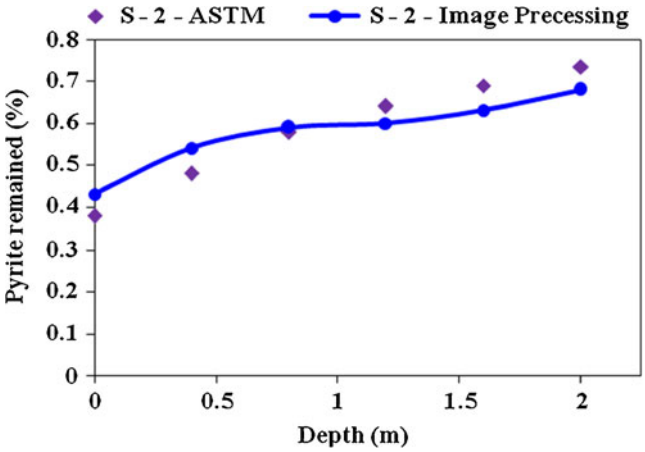

Fig. 8 Comparison of the image processing results (*solid line*) with the measured values (*dots*) for the amount of pyrite remained within the waste particles versus depth in trench no. 2

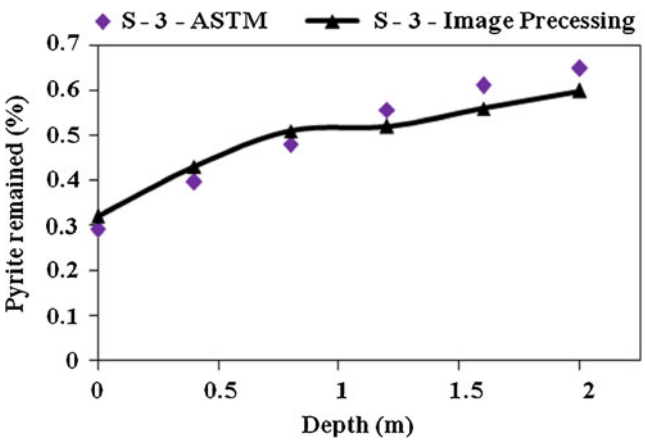

Fig. 9 Comparison of the image processing results (*solid line*) with the measured values (*dots*) for the amount of pyrite remained within the waste particles versus depth in trench no. 3

and volume percent (measured in the image processing method) of pyrite. All these matters are considered in the computations by multiplying a constant coefficient (k) in Eq. 10.

According to all these statements, the amount of k depends on various factors such as powder size (of which the polished sections were created), the hardness of waste materials and their density. In our investigation, the amount of k was set as 0.03030. This amount was found by comparing the results of image processing method and ASTM approach in samples of trench no. 1. The coefficient was then used for other samples. Figures 7, 8 and 9 compare the amount of measured pyrite (Table 1) with the amount of pyrite calculated by image processing approach at different depths of three trenches. It can be observed that the amount of pyrite that remained within the wastes at different depths of wastes (and therefore the pyrite oxidation rate) could be predicted by applying image processing approach. As Figs. 7, 8 and 9 show, the content of pyrite remained within the waste particles of the Alborz Sharghi coal washing waste pile increases gradually with depth which is because of the oxidation of pyrite in the shallower depths where oxygen is present in the pore spaces of the wastes. The relative error compared to ASTM method for each sample is shown in Table 1.

5 Conclusions

Information about the abundance, distribution and origin of sulphur in coal is important while sulphur oxides released in coal combustion are a major source of acid rain. Furthermore, oxidation of sulphide minerals (in particular pyrite as the most abundant sulphide mineral) resulting from the exposure of these minerals to both oxygen and water is the most important factor in producing acid mine drainage that might have a negative environmental impact on aquatic systems. Hence, pyrite content and its oxidation within the waste particles of the Alborz Sharghi coal washing waste pile were investigated. The most widely used method for measuring the amounts of different types of sulphur presented by the ASTM is a cumbersome method with a difficult preparation process. As an alternative, a new simple and direct method was employed, using image processing, for the determination of pyrite content in coal wastes. Providing visualised results is one of the important features of the presented method. Comparison of the image processing results with the measured values of pyrite amount that remained within the waste particles in different depths proves the ability of image processing approach for predicting the oxidation of pyrite in waste dumps. The results show that pyrite content within the wastes particles increases with depth which can be assumed as an evidence of the pyrite oxidation at the shallower depths where oxygen is available in the pore spaces of the wastes.

Acknowledgements The authors would like to thank the Alborz Sharghi Coal Company for supporting this research. The authors are grateful to the Faculty of Mining and metallurgy Engineering, Amirkabir University of Technology (Tehran Polytechnic) for the financial and technical support provided for the M.Sc. thesis of the first author.

References

1. Ward, C. R. (2002). Analysis and significance of mineral matter in coal seams. *International Journal of Coal Geology, 50*, 135–168.
2. Huggins, F. E. (2002). Overview of analytical methods for inorganic constituents in coal. *International Journal of Coal Geology, 50*, 169–214.
3. Chou, C. L. (1997). Geological factors affecting the abundance, distribution, and speciation of sulfur in coals. In Q. Yang (Ed.), *Proceedings of the 30th International Geological Congress. Geology of Fossil Fuels—Coal* (Vol. 18, pp. 47–57). Utrecht: VSP. Part B.
4. Barrie Johnson, D., & Hallberg, K. B. (2005). Acid mine drainage remediation options: a review. *The Science of the Total Environment, 338*, 3–14.
5. Gladfelter, W. L., & Dickerhoof, D. W. (1976). Use of atomic absorption spectrometry for iron determinations in coals. *Fuel, 55* (4), 360–361.
6. Aylmer, D. M., & Rowe, M. W. (1984). A new method for the simultaneous determination of pyrite content and proximate analysis in coal. *Thermochimica Acta, 78*, 81–92.
7. Shifeng, D., Xiaoqiang, H., Deyi, R., & Yuegang, T. (2003). Surface analysis of pyrite in the No. 9 coal seam, Wuda Coalfield, Inner Mongolia, China, using high-resolution time-of-flight secondary ion mass-spectrometry. *International Journal of Coal Geology, 55*, 139–150.
8. Bolin, T. B. (2010). Direct determination of pyrite content in Argonne premium coals by the use of sulfur X-ray near edge absorption spectroscopy (S-XANES). *Energy & Fuels, 24*(10), 5479–5482.
9. Querol, X., Alastuey, A., Chinchon, J. S., Fernandez Turiel, J. L., & Lopez-Soler, A. (1993). Determination of pyritic sulphur and organic matter contents in Spanish subbituminous coals by Xray powder diffraction. *International Journal of Coal Geology, 22*, 279–293.
10. Finkelman, R. B. (1981). Modes of occurrence of trace elements in coal. *U. S. Geological Survey Open-File Report, 81–99*, 312.
11. Finkelman, R. B. (1988). The inorganic geochemistry of coal: a scanning electron microscopy view. *Scanning Microscopy, 2*, 97–105.
12. Shirazi, A. R., & Lindqvist, O. (1993). An improved method of preserving and extracting mineral matter from coal by very low-temperature ashing (VLTA). *Fuel, 72*, 125–131.
13. Lengke, M., Davis, A., & Bucknam, C. (2010). Improving management of potentially acid generating waste rock. *Mine Water and the Environment, 29*(1), 29–44.
14. Cathles, L. M., & Apps, J. A. (1975). A model of the dump leaching process that incorporates oxygen balance, heat balance and air convection. *Metallurgical Transactions, B6*, 617–624.
15. Jaynes, D. B., Rogowski, A. S., & Pionke, H. B. (1984). Acid mine drainage from reclaimed coal strip mines, 2, simulation results of model. *Water Resources Research, 20*(2), 243–250.
16. Davis, G. B., Doherty, G., & Ritchie, A. I. M. (1986). A model of oxidation in pyritic mine wastes. Part 2: comparison of numerical

and approximate solutions. *Applied Mathematical Modelling, 10* (5), 323–329.
17. Davis, G. B., & Ritchie, A. I. M. (1986). A model of oxidation in pyritic mine wastes. Part 1: equations and approximate solution. *Applied Mathematical Modelling, 10*(5), 314–322.
18. Elberling, B., Nicholson, R. V., & Scharer, J. M. (1994). A combined kinetic and diffusion model for pyrite oxidation in tailings: a change in controls with time. *Journal of Hydrology, 157*(1), 47–60.
19. Singh, R. N., & Doulati Ardejani, F. (2004). Finite volume discretisation for solving acid mine drainage problems. *Archives of Mining Science, 49*(4), 531–556.
20. Doulati Ardejani, F., Jodieri Shokri, B., Moradzadeh, A., Soleimani, E., & Ansari Jafari, M. (2008). A combined mathematical geophysical model for prediction of pyrite oxidation and pollutant leaching associated with a coal washing waste dump. *International journal of Environmental Science and Technology, 5*(4), 517–526.
21. Doulati Ardejani, F., Jodeiri Shokri, B., Bagheri, M., & Soleimani, E. (2010). Investigation of pyrite oxidation and acid mine drainage characterization associated with Razi active coal mine and coal washing waste dumps in the Azad shahr–Ramian region, northeast Iran. *Environmental Earth Sciences, 61*, 1547–1560.
22. Atkins, A. S., & Pooley, F. D. (1982). The effects of biomechanisms on acidic mine drainage in coal mining. *International Journal of Mine Water, 1*, 31–44.
23. Doulati Ardejani, F., & Ziadin Shafaei, S. (2009). *Geoenvironmental modelling*. Shahrood: Shahrood University of Technology. In Persian.
24. Gerke, H. H., Molson, J. W., & Frind, E. O. (2001). Modelling the impact of physical and chemical heterogeneity on solute leaching in pyritic overburden mine spoils. *Ecological Engineering, 17*, 91–101.
25. Gonzalez, R. C., Woods, R. E., & Eddins, S. L. (2004). Digital Image Processing Using Matlab. Prentice Hall, 1–597.
26. Image Processing Toolbox™ User's Guide, MathWorks, Inc. (2008), 1–566.
27. Alley, R. E. (1996). Algorithm theoretical basis document for decorrelation stretch. Version 2.2. Jet Propulsion Laboratory. 4800 Oak Grove Drive, Pasadena, CA 91109.
28. Sadeghiamirshahidi, M., Eslam Kish, T., Doulati Ardejani, F. (2012). Application of artificial neural networks to predict pyrite oxidation in a coal washing refuse pile. *Fuel*. doi:10.1016/j.fuel.2012.10.016.